Coherent Array Imaging Using Phased Subarrays. Part II: Simulations and Experimental Results

Jeremy A. Johnson, *Student Member, IEEE*, Ömer Oralkan, *Student Member, IEEE*,
Sanlı Ergun, *Member, IEEE*, Utkan Demirci, *Student Member, IEEE*, Mustafa Karaman, *Member, IEEE*,
and Butrus T. Khuri-Yakub, *Fellow, IEEE*

Abstract—The basic principles and theory of phased subarray (PSA) imaging imaging provides the flexibility of reducing the number of front-end hardware channels between that of classical synthetic aperture (CSA) imaging—which uses only one element per firing event—and full-phased array (FPA) imaging—which uses all elements for each firing. The performance of PSA generally ranges between that obtained by CSA and FPA using the same array, and depends on the amount of hardware complexity reduction. For the work described in this paper, we performed FPA, CSA, and PSA imaging of a resolution phantom using both simulated and experimental data from a 3-MHz, 3.2-cm, 128-element capacitive micromachined ultrasound transducer (CMUT) array. The simulated system point responses in the spatial and frequency domains are presented as a means of studying the effects of signal bandwidth, reconstruction filter size, and subsampling rate on the PSA system performance. The PSA and FPA sector-scanned images were reconstructed using the wideband experimental data with 80% fractional bandwidth, with seven 32-element subarrays used for PSA imaging. The measurements on the experimental sector images indicate that, at the transmit focal zone, the PSA method provides a 10% improvement in the 6-dB lateral resolution, and the axial point resolution of PSA imaging is identical to that of FPA imaging. The signal-to-noise ratio (SNR) of PSA image was 58.3 dB, 4.9 dB below that of the FPA image, and the contrast-to-noise ratio (CNR) is reduced by 10%. The simulated and experimental test results presented in this paper validate theoretical expectations and illustrate the flexibility of PSA imaging as a way to exchange SNR and frame rate for simplified front-end hardware.

I. Introduction

IN the companion paper [1], phased subarray imaging was presented as a method for significantly reducing the number of costly and bulky front-end electronic channels in a phased-array imaging system. Conventional full-phased array (FPA) imaging transmits and receives on all transducer elements simultaneously to form each beam of a sector scan. The number of front-end electronic channels required is equal to the number of transducer elements. On the other extreme, classical synthetic aperture (CSA) imaging transmits and receives on only one element at a time. Phased subarray (PSA) performs consecutive transmit and receive acquisitions on a number of small subarrays that span the full array. The number of front-end electronic channels required for the PSA system is reduced to the number of elements per subarray. Due to the reduced transmit and receive aperture size, a smaller number of beams need be acquired as determined by the Nyquist sampling criteria. The unacquired beams are reconstructed by upsampling and interpolating with a subarray-dependent digital filter. The weighted coherent sum of the subarray responses equals that of an FPA system. Because FPA imaging uses all elements simultaneously during both transmit and receive, we use it as the gold-standard imaging method to which we compare PSA imaging.

The remainder of the paper is organized as follows: Section II describes the methods used to acquire the experimental pulse-echo data, generate the simulated A-scan data, and process the data to form images. Section III describes the results obtained using a narrowband and wideband PSA reconstruction filter and compares the results to an FPA system. Concluding remarks are given in Section IV.

II. Methods

A. Experimental Data

The experimental setup and methods used to acquire the raw radio frequency (RF) pulse-echo data for this work was reported in detail by Oralkan *et al.* [2]. The experimental A-scans were acquired with a one-dimensional (1-D), linear, capacitive micromachined ultrasound transducer array. The array consisted of 128 elements with a pitch of 250 μm. Each element was 6 mm × 0.2 mm in size and consisted of 750 capacitive micromachined ultrasound transducer (CMUT) cells electrically connected in parallel. Custom front-end hardware was designed and built for acquiring pulse-echo data. A 40-V direct current (DC) bias

TABLE I
SYSTEM PARAMETERS.

Parameter	Experimental	Simulated
Number of array elements (N)	128	128
Element pitch (d)	250 μm	250 μm
Center frequency (f_0)	3.0 MHz	3.0 MHz
6-dB Bandwidth (narrowband)	5%	5%
6-dB Bandwidth (wideband)	80%	80%
Sampling frequency (f_s)	50 MHz	96 MHz
Velocity of sound (c)	1430 m/s	1430 m/s
Location of point reflector	13.1 cm[1]	13.1 cm

[1]Fourth wire target.

TABLE II
BEAMFORMER SETTINGS.

Parameter	Narrowband	Wideband
Number of FPA/CSA beams (Q_{FPA})	185	361
Number of PSA beams (Q_{PSA})	47	91
Scan angle (Θ)	90°	90°
Number of subarrays (K)	7	7
Number of elements per subarray (M)	32	32
Upsampling rate	4	4
Sampling frequency (output beams)	12 MHz	12 MHz
Transmit focal depth	13.1 cm	13.1 cm

was applied to the array, and a 15-V, 100-ns unipolar pulse was applied to generate the transmit pulse. The received signals were amplified with a fixed gain of 60 dB, then sampled at 50 MHz. In general, sampling at a rate of 32 times the center frequency eliminates delay quantization errors. Because 50 MHz represents sampling at roughly 16 times the center frequency, there is a possibility that the delay quantization error will affect the reconstructed images of all imaging methods. The A-scans were formed by transmitting on a single element, then receiving from all other elements and storing the received signals individually. The weak transmit power due to transmitting on only a single element was compensated for by recording the average of 100 received signals with 12-bit resolution, resulting in a 20-dB signal-to-noise ratio (SNR) gain. In addition, a 1–5 MHz digital bandpass filter was applied to all A-scans.

The test phantom consisted of seven parallel steel wires submersed in vegetable oil, which protects the array electronic wiring from corrosion and mimics the acoustic properties of tissue better than water [2]. The wires had a diameter of 0.38 mm and were uniformly spaced with a separation of 2.85 cm. We analyzed the reflected signal from one of the wire targets; the center frequency of the response was 3.0 MHz, with a 6-dB bandwidth of 80%, which was not compensated for diffraction or attenuation losses [2]. The parameters for the experimental system are listed in Table I.

B. A-Scan Simulations

A computer program was written to generate A-scans similar to those acquired from the experimental setup, simulating both the transducer array and wire phantom geometries. A point reflector was located 13.1 cm (f/# = 4.1) from the array, the distance to the fourth wire target in the experimental setup. The excitation pulse used was a modulated Gaussian. Loss due to radiation was included in the model; attenuation and electronic noise were not included. As with the experimental A-scans, a 1–5 MHz digital bandpass filter was applied. Unless otherwise mentioned, the settings used to generate the simulated A-scans are as listed in Table I.

C. Beamformer

Custom RF beamforming software was written to generate all images. The RF beamformer used the standard delay-and-sum method to calculate the image intensity, and applied fixed transmit focusing and dynamic receive focusing. The transmit focal distance was 13.1 cm (f/# = 4.1). The image intensity was calculated at uniformly spaced points along each of Q beams with an output sampling rate of 12 MHz. The beams all radiated from the center of the array and were evenly spaced in $\sin\theta$ and spanned a sector angle of Θ. Nearest-neighbor interpolation was used to determine which A-scan sample contributed to each image sample. A minimum f/# of 2 was used for both the transmit and receive apertures, although all image targets used in this study are beyond this range. Unless otherwise specified, the beamformer settings used to produce the results reported in this paper are listed in Table II.

D. Image Formation

The remaining steps used to form the ultrasound images were performed using Matlab (The Mathworks, Natick, MA). The beams were treated as the real part of an analytic signal. The complex signal was generated by applying the Hilbert transform [3]. For FPA and CSA imaging, these beams were immediately envelope detected to form the final image. The PSA imaging required additional reconstruction steps prior to envelope detection, as described below. Envelope detection of the beams was performed by calculating the magnitude of the complex analytic signal. For images in $r - \sin\theta$ format, the beams are displayed directly without scan conversion. Bilinear interpolation was used to scan convert the experimental image data displayed in rectangular coordinates [4].

The details of PSA image formation and reconstruction filter design were previously described [1], and the steps taken are summarized here. Each low-resolution subarray image was first laterally upsampled by L by inserting zero-sampled beams. To reconstruct the beams, a 1-D (for narrowband systems) or 2-D (for wideband systems) finite-impulse response (FIR) filter was convolved with each subarray image, producing the high-resolution subarray images. The 2-D filters have N_q taps in the lateral dimension

TABLE III
PSA IMAGING PARAMETERS.

Parameter	Value
PSA upsampling rate (L)	4
Filter lateral width (N_q) (narrow- and wide-band filters)	31
Filter axial height (N_r) (wideband filter only)	31
Window function (lateral and axial)	Hamming

and N_r taps in the axial dimension. In the lateral dimension, this corresponds to using the nearest eight acquired beams to reconstruct the others. The high-resolution subarray images are coherently weighted and summed to form the final PSA image. Unless otherwise specified, the PSA system parameters used to produce the results reported in this paper are listed in Table III.

E. Spatial Resolution

Spatial resolution measurements were made using $r - \sin\theta$ images of each wire target. Sampling rates were increased by 4 laterally and 10 axially, resulting in sample spacing of $\Delta\sin\theta = 0.001$ ($\Delta\theta = 0.05°$ at $\theta = 0°$) laterally and 6 μm axially. Spline interpolation was used to calculate the spatial resolution along both axes.

F. Image Signal-to-Noise Ratio

The SNR measurements were made using experimental images after scan conversion. The SNR was calculated for each of the six targets. An $r - \sin\theta$ image centered around the target was formed with dimensions of 45° laterally and 2.6 cm axially. The signal power (s^2) was calculated as the square of the maximum point-spread function (PSF) magnitude, and the noise power (σ^2) was calculated as the variance of the noise in the area around the PSF. The image SNR then was calculated as $SNR = 10\log\left(s^2/\sigma^2\right)$.

G. Contrast-to-Noise Ratio

The contrast-to-noise ratio (CNR) of an imaging system indicates how well it can distinguish regions with different densities of scatterers. Two cysts were simulated for CNR measurements: one with a 4-mm diameter and the other with an 8-mm diameter. Each was placed along the normal of a 120-element array at a depth of 10 cm. Point reflectors were randomly distributed with a density of 15-points/mm^2 in the region surrounding the cyst. 30°-lateral × 2-cm-axial images were used for CNR measurements. The transmit focal distance was located at the center of the cyst.

The CNR was calculated from 60-dB images as $CNR = |\mu_c - \mu_s|/\sigma_s$, where μ_c and μ_s are the mean image intensities of the cyst and speckle regions, respectively, and σ_s is the standard deviation of the image intensity in the speckle region [5]. For the 4-mm cyst, the central 3-mm diameter portion was used to calculate the mean, and all points

beyond a 5-mm diameter were used as the speckle region. For the 8-mm cyst, these boundaries were defined by 6-mm and 10-mm diameters.

III. RESULTS

A. Narrowband Reconstruction

The parameters used for simulated and experimental narrowband images are given in Tables I, II, and III. Fig. 1 outlines the cosubarray responses at each step of a simulated narrowband system. The response at each stage was similar to the theoretical response shown in Fig. 8 of [1]. The cosubarray responses are given in Fig. 1(a); the cosubarrays filled the range of lateral spatial frequency, indicating that beamspace was critically sampled. Upsampling the beams in the spatial domain by four led to the desired response and three aliases, as shown in Fig. 1(b). Due to the truncation and windowing of the reconstruction filter in the spatial domain, the PSA reconstruction filters (dashed line) had a smooth roll-off that limited their ability to perfectly suppress the aliases. Energy from adjacent aliases was evident in the cosubarray response after reconstruction [Fig. 1(c)], resulting in ripples in the final coarray response [Fig. 1(d)]. Regardless, the final PSA response closely resembled the FPA response.

The process was repeated using the experimental data, and the results are illustrated in Fig. 2. The primary difference in the response compared to that of the simulated data was the addition of noise for both FPA and PSA imaging. Although the final PSA coarray response approximated that of FPA imaging, the expected decrease in the SNR was clearly evident. Unlike the FPA response, the PSA final coarray had higher noise contributions near the center—corresponding to lower lateral spatial frequencies. This result is expected as that PSA imaging acquires fewer independent samples at lower spatial frequencies compared to FPA imaging.

B. Wideband Reconstruction

The settings for wideband simulations are shown in Tables I, II, and III. We first illustrate the 2-D frequency response of wideband PSA and FPA systems using simulated 80% bandwidth data in Fig. 3. The 2-D frequency response of acquired subarray images, the upsampled images, and the reconstruction filter are shown for four different subarrays ($k = 1\ldots4$) in Fig. 3(a)–(c). The response of the remaining three subarrays ($k = 5\ldots7$) are not shown as they were symmetric to those of the first three subarray responses. The overall magnitude response can be seen in the mesh plot for the first subarray in Fig. 3(f)–(h). The overall PSA response is compared to the FPA response in Fig. 3(d) and (e). Only the positive temporal frequency is displayed because the signal is analytic and has zero energy in the negative axial spatial frequency (temporal frequency) domain. The spatial frequency response of a
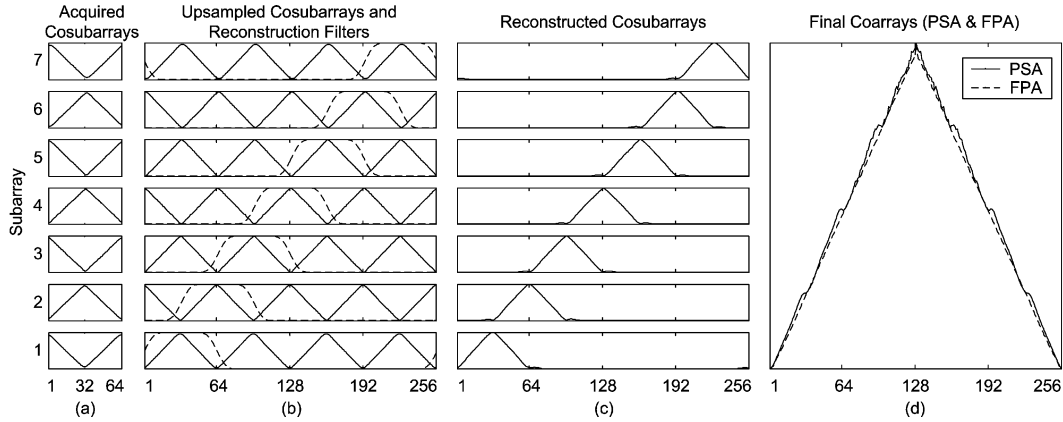
Fig. 1. Coarray representation of narrowband PSA image acquisition and reconstruction based on simulated data with 5% bandwidth and 1-D lateral spatial filtering. (a) Cosubarray corresponding to critically-sampled beam acquisition. (b) Upsampling in beamspace by a factor of four leads to replication in coarray space. The 31-tap filter response shown by the dotted line is centered over the desired cosubarray response; all others are unwanted aliases. (c) After reconstruction, the cosubarrays approximate the response of a fully-sampled beamspace. (d) By weighting and summing these responses, the final PSA coarray closely approximates that of FPA imaging. The vertical scale in all plots is the magnitude of the lateral spatial frequency response.
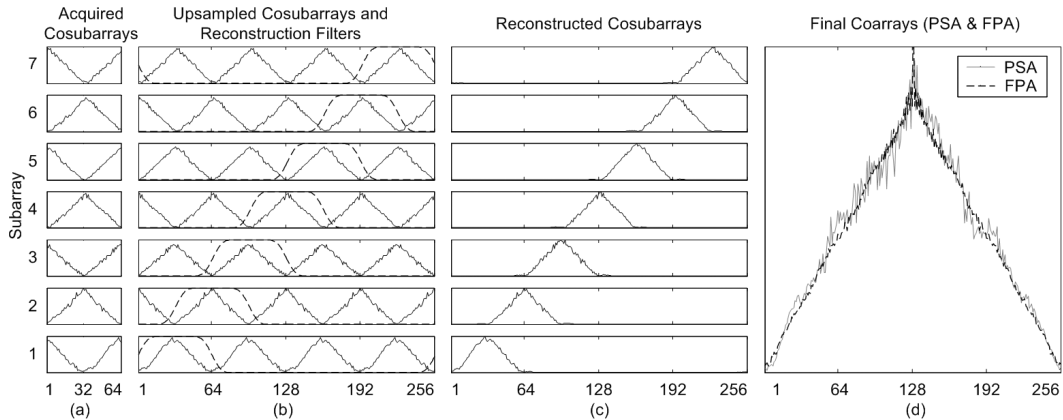

Fig. 2. Coarray representation of narrowband PSA image acquisition and reconstruction based on experimental data with 5% bandwidth and 1-D lateral spatial filtering. (a) Cosubarray corresponding to critically-sampled beam acquisition. (b) Upsampling in beamspace by a factor of four leads to replication in coarray space. The 31-tap filter response shown by the dotted line is centered over the desired cosubarray response; all others are unwanted aliases. (c) After reconstruction, the cosubarrays approximate the response of a fully-sampled beamspace. (d) By weighting and summing these responses, the final PSA coarray closely approximates that of FPA imaging. The vertical scale in all plots is the magnitude of the lateral spatial frequency response.

phased array system has compact support, and specifying the passband for the reconstruction filter requires knowing the bounds of this support. For this reason, the responses are displayed on a logarithmic scale such that even regions with weak (though important) signal power are visible. Note the similarity of these responses to the theoretical drawings (Fig. 9 in [1]).

We investigated the performance of the narrowband and wideband reconstruction filters using simulated data with fractional bandwidth ranging from 10% to 90%, as shown in Fig. 4. For all imaging methods, the axial width of the main lobe decreased with increasing bandwidth as expected. The 2-D PSFs resulting from applying the wideband filter were in excellent agreement with those obtained from FPA imaging and exhibit minimal distortion.

Compared to the 2-D wideband filter, the 1-D narrowband filter has a lower image reconstruction complexity—

as measured in number of operation counts required for image reconstruction—due to many fewer filter taps. Therefore, it is desirable to use the narrowband filter whenever the system signal bandwidth permits. The narrowband PSA filter performed more poorly than the wideband PSA filter at all bandwidths. The narrowband PSF became more distorted with increasing bandwidth. For the bandwidths studied, the distortions caused by narrowband PSA reconstruction were minimal at bandwidths of 50% and below.

C. PSA System Design Parameters

As compared to a conventional FPA imaging system, a PSA system adds several additional system parameters that must be considered when designing the system. These additional parameters include the size of each subarray
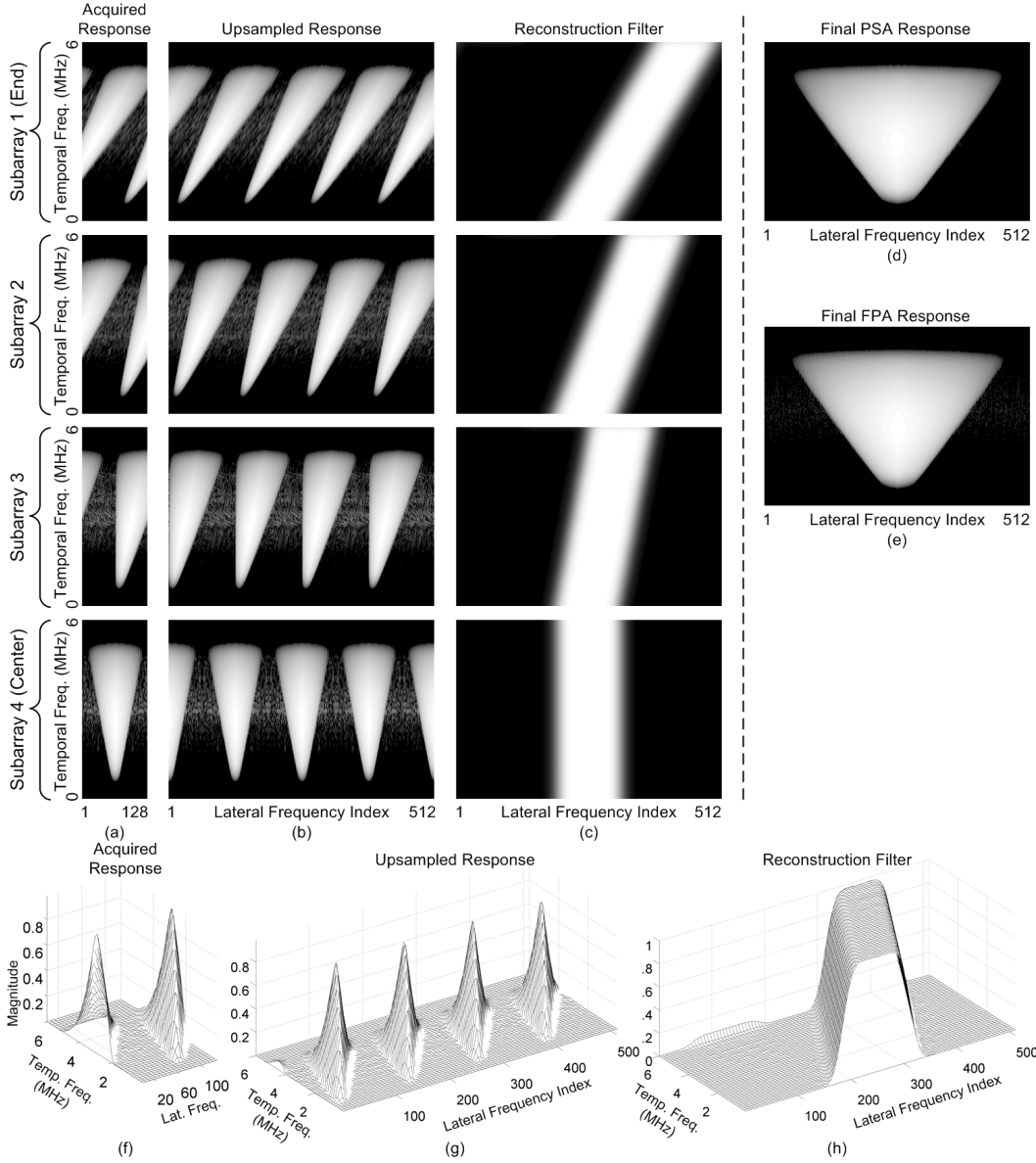
Fig. 3. 2-D frequency responses of a simulated 3 MHz, 80% bandwidth phased array ultrasound system. (a) Responses of subarrays 1–4 for a PSA system when acquired with a low beamrate. (b) Upsampling the subarray images by a factor of four produces a center desired response and three unwanted aliases. (c) The passband of the subarray-dependent reconstruction filter preserves the desired response while suppressing the aliases. (d) The reconstructed subarray images are weighted and summed, resulting in a response equivalent to that of a FPA system shown in (e). (The images in (c) are displayed with a linear scale; all other images are displayed with 50 dB of log compression.) Mesh plots of the second subarray response are shown in (f), (g), and (h).

(equivalently, the number of subarrays), the number of beams to acquire for each subarray image, the upsampling rate, and the size of the reconstruction filter. The relationship between these parameters is discussed in [1]. Unless otherwise stated, the default design parameters used in this study are summarized in Tables II and III and were chosen to achieve good performance without excess computational complexity for image reconstruction.

Several simulations were performed to illustrate the impact on PSA system performance when compromising each of several design parameters: filter size, upsampling rate, subarray size, focal depth. One parameter was varied in each simulation and all others were held constant to their default values listed in Tables II and III. To compare the

performance of each system, we generated $r - \sin\theta$ images of the point spread function, as well as the magnitude of the 2-D fast Fourier transform (FFT) of the PSF prior to envelope detection.

1. Filter Size: We tested the performance when varying the filter lateral width and axial height independently. For each case, the same passband was defined in the frequency domain, but the spatial-domain filter was truncated and windowed to the size specified.

The spatial PSA reconstruction filter was tested with 7, 15, 23, and 31 taps laterally, as shown in Fig. 5. These filter sizes correspond to using the nearest 2, 4, 6, and 8 acquired beams for interpolation. The PSFs became sig-
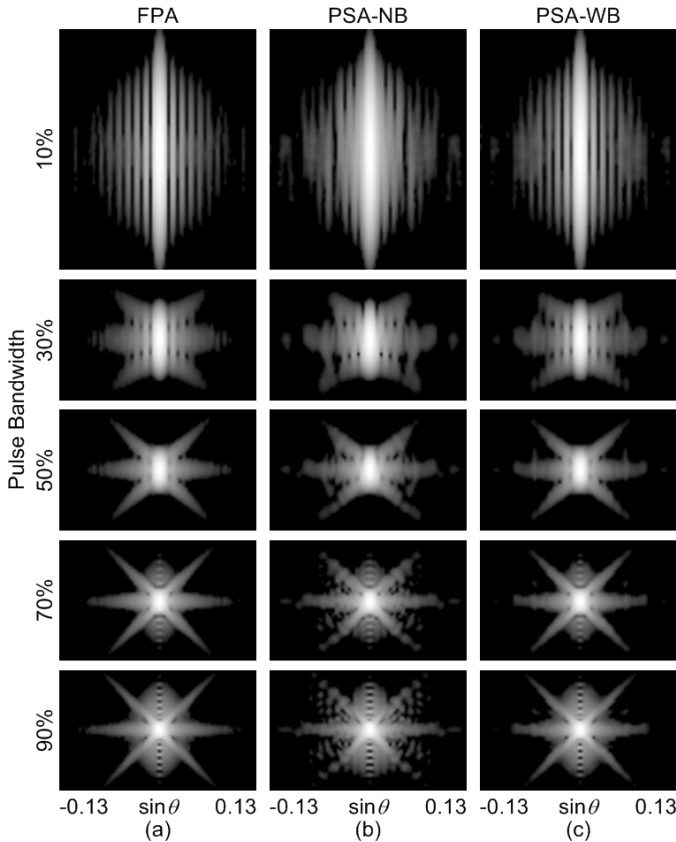
Fig. 4. Point spread functions from the simulated data illustrating the effect of varying the signal bandwidth on (a) the gold-standard FPA imaging method, (b) PSA narrowband imaging with a 1-D lateral reconstruction filter; and (c) PSA wideband imaging with a 2-D reconstruction filter. The $r - \sin\theta$ images are 15° wide, and displayed with 60 dB of log compression. The 10% bandwidth images are 6.4 mm high; all others are 3.2 mm.
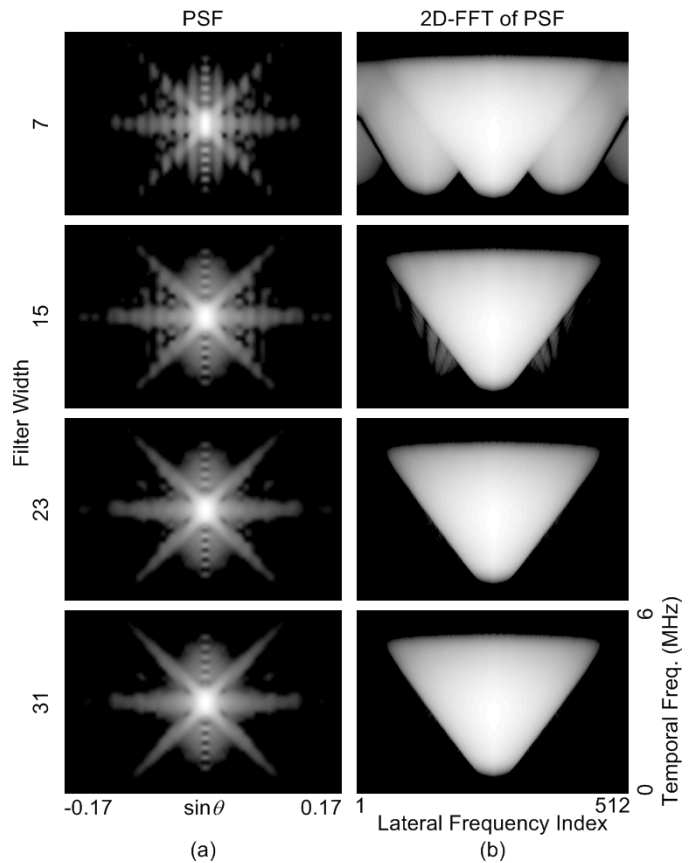

Fig. 5. (a) Point spread functions and (b) frequency responses of the simulated data illustrating the effect of varying the 2-D wideband PSA reconstruction filter width (number of taps in the lateral dimension). The $r - \sin\theta$ images are 3.4 mm high and 20° wide. The PSF and FFT images are displayed with 60 dB and 50 dB of log compression, respectively.

nificantly degraded for filter widths below 23 taps. There were minimal perceptible differences between the results of the 23- and 31-tap filters, and we observed no perceptible differences for filter widths exceeding 31 taps. Insufficiently narrow filters were unable to suppress the aliases in the frequency domain as illustrated in Fig. 5(b).

The filter also was tested with 7, 15, 23, and 31 taps axially, as shown in Fig. 6. No differences were observable for filters exceeding 23 taps. The filter length determines how much of a slope the passband will have in the frequency domain [as illustrated in Fig. 3(c)]. Therefore, it is not surprising that the PSF resulting from the use of a 2-D filter with only seven taps in the axial dimension was remarkably similar to that of the narrowband filter—which has only one tap in the axial dimension—when used for wideband systems [Fig. 4(b)]. Note that both the narrowband and wideband filters had 31 taps in the lateral dimension.

2. Upsampling Rate: Fig. 7 illustrates the results of upsampling by rates of 3, 4, 5, and 6. For each of these upsampling rates, we varied the lateral width of the reconstruction filter such that eight acquired beams were used for interpolation; the widths were 23, 31, 39, and 47, respectively. Distortions were clearly visible for all upsam-

pling rates above the critical rate of 4, and upsampling at a lower rate caused no visually perceptible improvement. Therefore, it is not worth sacrificing the frame rate in hopes of achieving better results from a reduced upsampling rate.

3. Subarray Size: One of the primary advantages of PSA imaging is that system parameters such as frame rate or image SNR can be traded for a substantial reduction in the front-end hardware complexity. To illustrate this flexibility, we tested the performance of PSA imaging using a 120-element array divided into subarrays ranging in size from 8 to 60 elements, equivalent to reducing the front-end hardware complexity over a range of 15 to 3. Because the upsampling rate was different for each case (ranging from 15 to 2), the lateral filter width was adjusted such that a fixed number (eight) of nearest acquired beams was used to reconstruct each interpolated beam. The lateral filter width varied from 119 to 15 taps.

The resulting PSFs are shown in Fig. 8. For subarrays having at least 20 elements, the differences in the PSF were minimal. Outer side lobes began to appear for subarrays with 12 or fewer elements. The response of these small subarrays was very narrow, leading to difficulties in designing
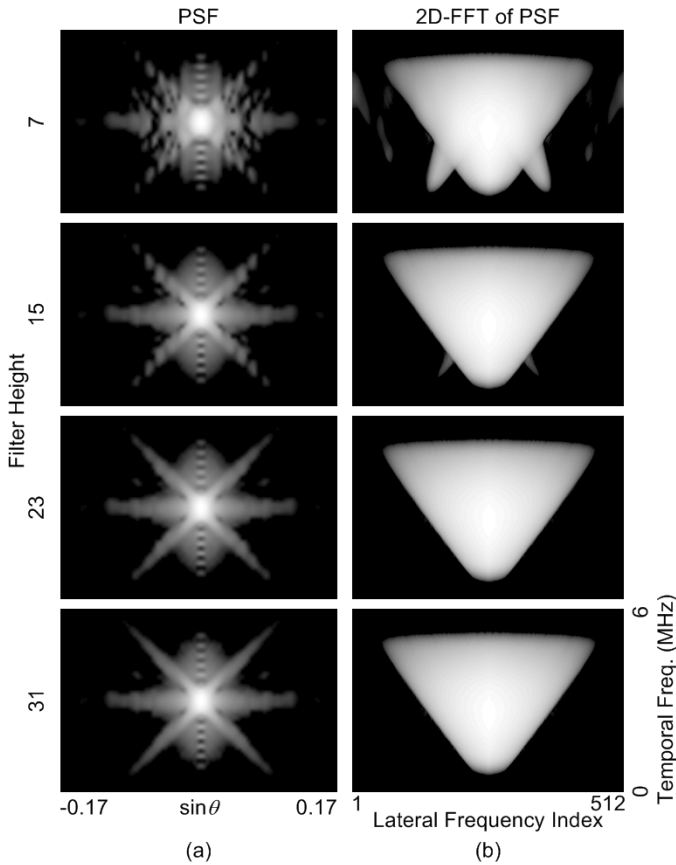
Fig. 6. (a) Point spread functions and (b) frequency responses from the simulated data illustrating the effect of varying the 2-D wideband PSA reconstruction filter height (number of taps in the radial dimension). The $r - \sin\theta$ images are 3.4 mm high and 20° wide. The PSF and FFT images are displayed with 60 dB and 50 dB of log compression, respectively.
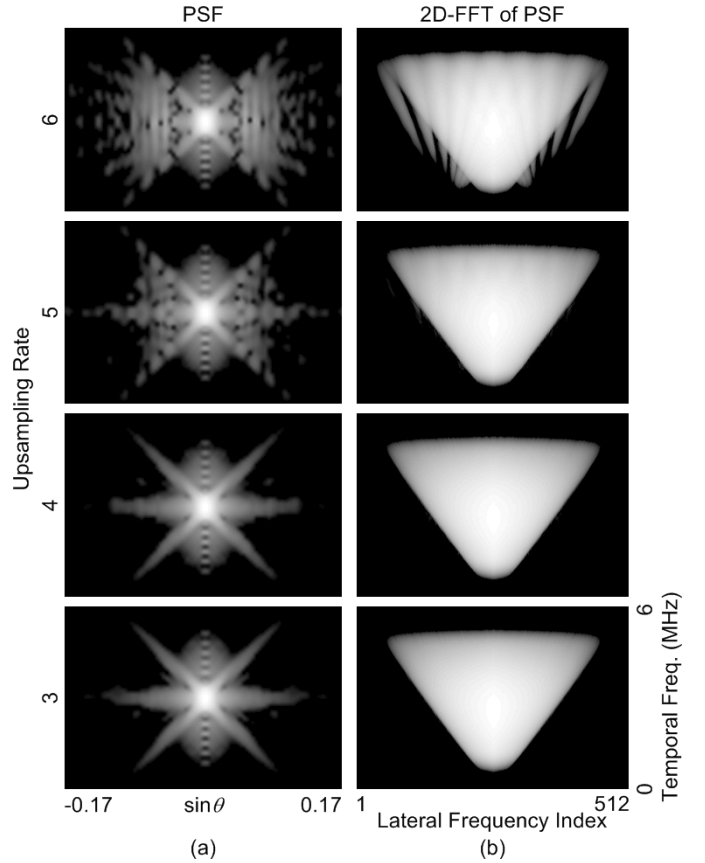

Fig. 7. (a) Point spread functions and (b) frequency responses from the simulated data illustrating the effect of varying the upsampling rate of the subarray images prior to reconstruction. The $r - \sin\theta$ images are 3.4 mm high and 20° wide. The PSF and FFT images are displayed with 60 dB and 50 dB of log compression, respectively.

reconstruction filters with sufficiently rapid roll-off and a uniform passband.

4. Focal Depth: All PSFs presented thus far were located at the transmit focal distance. The loss of resolution and other distortions that occur outside the transmit focal region are of serious concern when designing a real-time ultrasound system, and is an ongoing area of research [6]–[12]. The PSA point response at five different depths is given in Fig. 9 and is compared to that of FPA. At depths of 13.1, and 15.4 cm, the PSA response is very similar to the FPA response. The other three points further from the focal point show that the PSF for PSA imaging is significantly different from that of FPA. Although the PSF appears degraded due to the additional arms, the images also show that the energy in the original horizontal and diagonal arms has been reduced. The PSF of PSA imaging matches that of FPA imaging at the focal distance, and the similarity decreases with increasing distance from the focus.

5. Subarray Size and CNR: The CNR was measured using the simulated cyst phantom data as discussed in Section II-G and the results are presented in Fig. 10. Sample

sector-scanned images are shown in Fig. 10(a)–(f). The PSA images in Fig. 10(b) and (e) were formed using seven 30-element subarrays. All CNR measurements normalized to the FPA result are plotted in Fig. 10(g)–(h). For the 4-mm cyst, the CNR measurement of all but the two smallest subarray sizes were within 10% of the FPA measurement, and all were within 20%. Overall the CNR improved with increasing subarray size.

D. Experimental Results

1. Imaging Results: The full set of experimental A-scans were processed using both FPA and PSA imaging to create the 90° sector-scan images shown in Fig. 11(a) and (b). The settings used to generate the images are given in Tables I, II, and III. The points in the PSA image were slightly wider than those in the FPA image. For targets outside the focal region, the diagonal arms were blurred in the PSA image as discussed in Section II-C,4.

Close-ups of the fourth wire target are shown in Fig. 11(c) and (d) for FPA and PSA, respectively. Recall that the transmit focal depth was located at this target. The general shape of the PSF was similar to those from the simulations. The reader should keep in mind that these images are presented in rectangular coordinates, causing
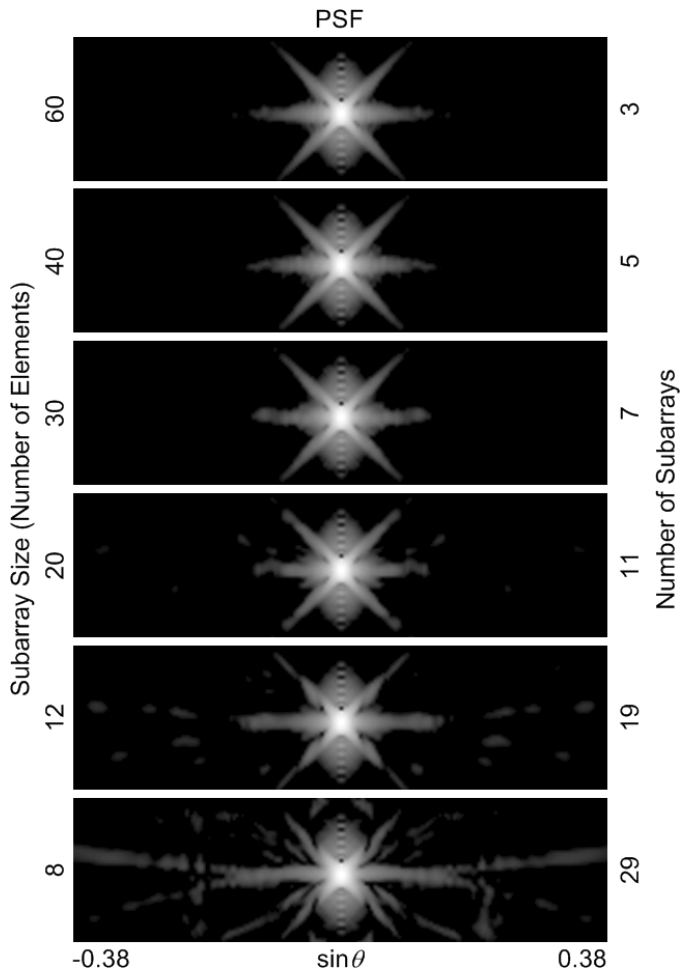
Fig. 8. Point spread functions from the simulated data using different subarray sizes (and equivalently, the number of subarrays). The $r - \sin\theta$ images are 3.4 mm high, 45° wide, and displayed with 60 dB of log compression.

Fig. 9. Response of the (a) FPA and (b) PSA systems for points at various depths around a fixed focal depth of 13.1 cm. The $r - \sin\theta$ images are 3.4 mm high, 15° wide, and displayed with 60 dB of logarithmic compression.

a slight upward curvature and different aspect ratio when compared to the simulated $r - \sin\theta$ images. One noticeable difference between these point responses and those obtained from the simulations is the appearance of additional lobes in the axial direction. These are due to crosstalk between array elements [2].

The close-up images are shown with 40-, 50-, and 60-dB of log compression, which were on either side of the noise floor for both imaging methods; 40 dB was above the noise floor of both methods, and thus no background noise was visible. The central lobe of the point responses for the two methods had a similar shape and size, but the left horizontal and upper-right diagonal arms were lengthened in the PSA response. At 50 dB, the FPA image was relatively noise free, but noise began to appear in the PSA image; this was because the noise floor for FPA was still below 50 dB, and that of PSA was just above 50 dB. In this case, the point response arms did not seem different in length, but were slightly wider in the PSA case. This result was not observed in the simulations and is likely due to the additive noise. At 60 dB, the dynamic range approached the noise floor of FPA and was well below that of PSA. Inde-
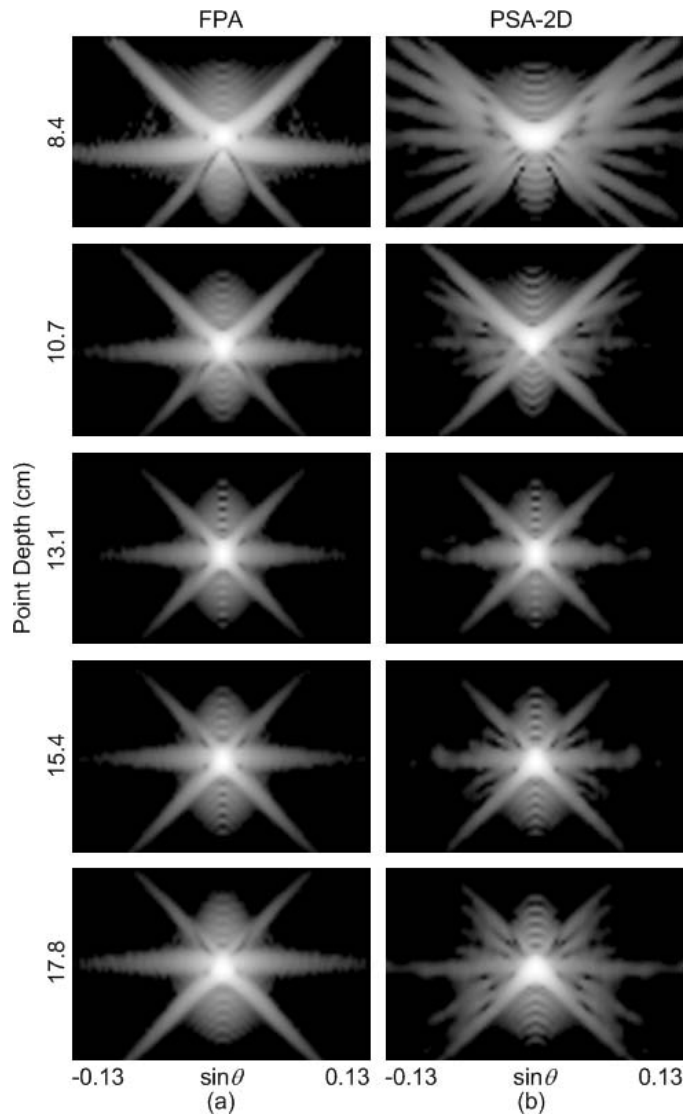
pendent of background noise, the two responses were similar without any major differences. Within the focal region, PSA imaging produced results equivalent to FPA imaging with an additional noise contribution. The increase of the noise level for PSA imaging was expected [1] and is further discussed in Section III-D,3.

Lateral and axial profiles of the point response are shown in Fig. 11(e) and (f). Compared to FPA, the lateral profile for PSA had a slightly increased noise floor. The shape of the main lobe base differed, but the width of the main lobe was in good agreement. The axial profiles were also remarkably similar, as seen in Fig. 11(f). The 6-dB resolution of the fourth wire target image was measured for both imaging methods. For FPA, the resolution was measured as 0.86° laterally and 0.31 mm axially; the PSA lateral and axial resolutions were 0.77° and 0.31 mm, respectively. The axial resolution for the two
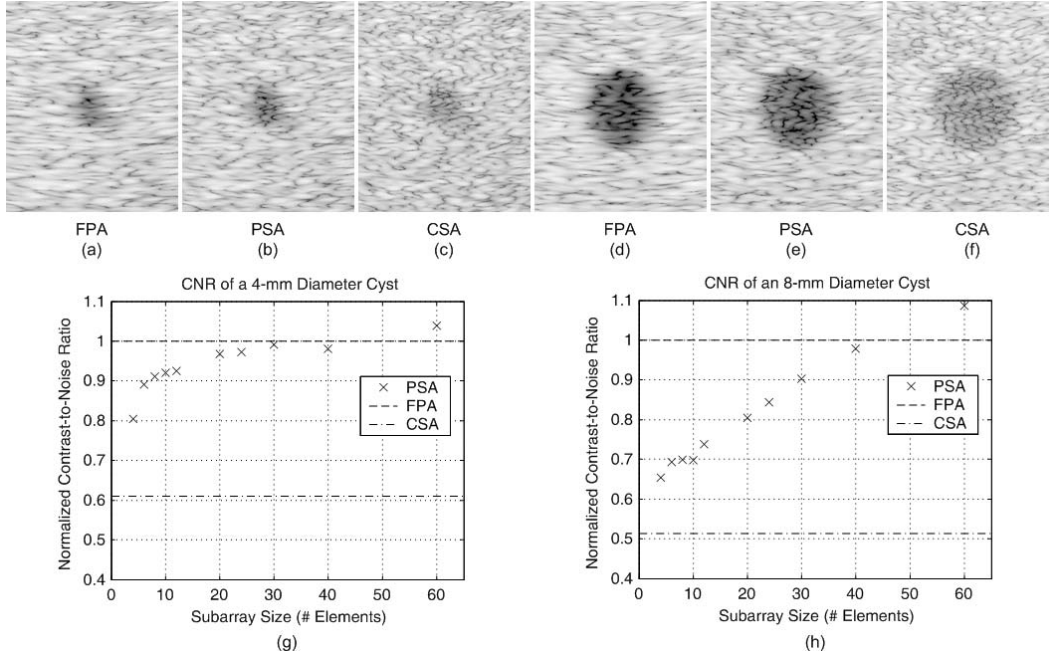
Fig. 10. Comparison of CNR for FPA, PSA, and CSA imaging methods using a simulated speckle phantom. (a)–(c) Sector scanned images for the 4-mm diameter cyst. (d)–(f) Sector scanned images for the 8-mm cyst. (a)–(f) are displayed with 50 dB dynamic range (b) and (e) are formed using seven 30-element subarrays. (g) and (h) CNR of the three methods normalized to FPA.

methods are identical, and the lateral resolution for PSA imaging is 10% less than that of FPA. This improvement in the lateral resolution was limited to the region near the focal zone, demonstrated when comparing the resolution for all six targets in the image. The mean axial and lateral resolutions for all points using FPA imaging were 0.33 mm ($\sigma = 0.04$ mm) and 1.1° ($\sigma = 0.2°$); PSA imaging achieved mean resolutions of 0.32 mm ($\sigma = 0.03$ mm) and 1.6° ($\sigma = 1.1°$). As before, the axial resolution was unaffected by PSA imaging. The large standard deviation of the lateral resolution measurement was due to the poor performance of both methods outside the focal region.

Theory did not predict that PSA imaging would attain higher lateral resolution than FPA imaging as measured at the focal point. The improved lateral resolution indicates that the PSA frequency response consisted of higher lateral spatial frequency components than the FPA frequency response. One possible cause is imperfect alias suppression, resulting in artifacts outside the theoretical bound of the 2-D frequency response. Another cause may be that the PSA coarray had increased response at the higher lateral spatial frequencies relative to the FPA coarray due to nonuniform interpolation filter passbands.

The SNR was measured at all six target locations. The mean SNR was 63.1 dB ($\sigma = 5.6$ dB) for FPA and 58.2 dB ($\sigma = 5.5$ dB) for PSA, representing only a 4.9 dB difference. These measurements agree well with the level of the noise floor of the lateral PSF shown in Fig. 11(e), and also explains the difference in noise levels between the two 60-dB images in Fig. 11(c)–(d).

The mean CNR of the 4-mm diameter cyst was 3.4 for both FPA and PSA; for the 8-mm cyst, the CNR for FPA

and PSA was 5.4 and 4.8, respectively. This represents a 10% decrease in CNR of PSA as compared to FPA.

These results are summarized in Table IV. The number of firings and frame rate were calculated assuming a 90° sector scan. In summary, this PSA system exchanges 5 dB of SNR and 10% CNR for a fourfold reduction in front-end hardware complexity.

2. Subarray Size and Resolution: To further illustrate the flexibility in PSA system design, we tested its performance with different numbers of subarrays using the experimental data from the center 120 elements of the array. We compared the resulting 6-dB axial resolution, lateral resolution, and image SNR to those of FPA and CSA, as shown in Figs. 12 and 13.

Lateral and axial resolution measurements are shown in Fig. 12. All results are shown normalized to the average of the FPA results at all targets. The CSA also is shown relative to FPA, and also was averaged across all targets. For PSA imaging, the mean is plotted with error bars representing one standard deviation away from the mean. Fig. 12(c) compares the averaged results for all subarray images at each target location. The small error bars at targets 3 to 6 indicate that all subarray sizes have consistent performance near the focal region. The PSA lateral resolution at targets 4 to 6 were smaller than that of FPA, consistent with the previous findings for the 128-element array. The lateral resolution as a function of the subarray size—and averaged over all target locations—is shown in Fig. 12(a). The mean PSA lateral resolution was larger than FPA for all subarray sizes due to the influence of the poor resolution in the near field, and the variation was large due to the large difference in resolutions between
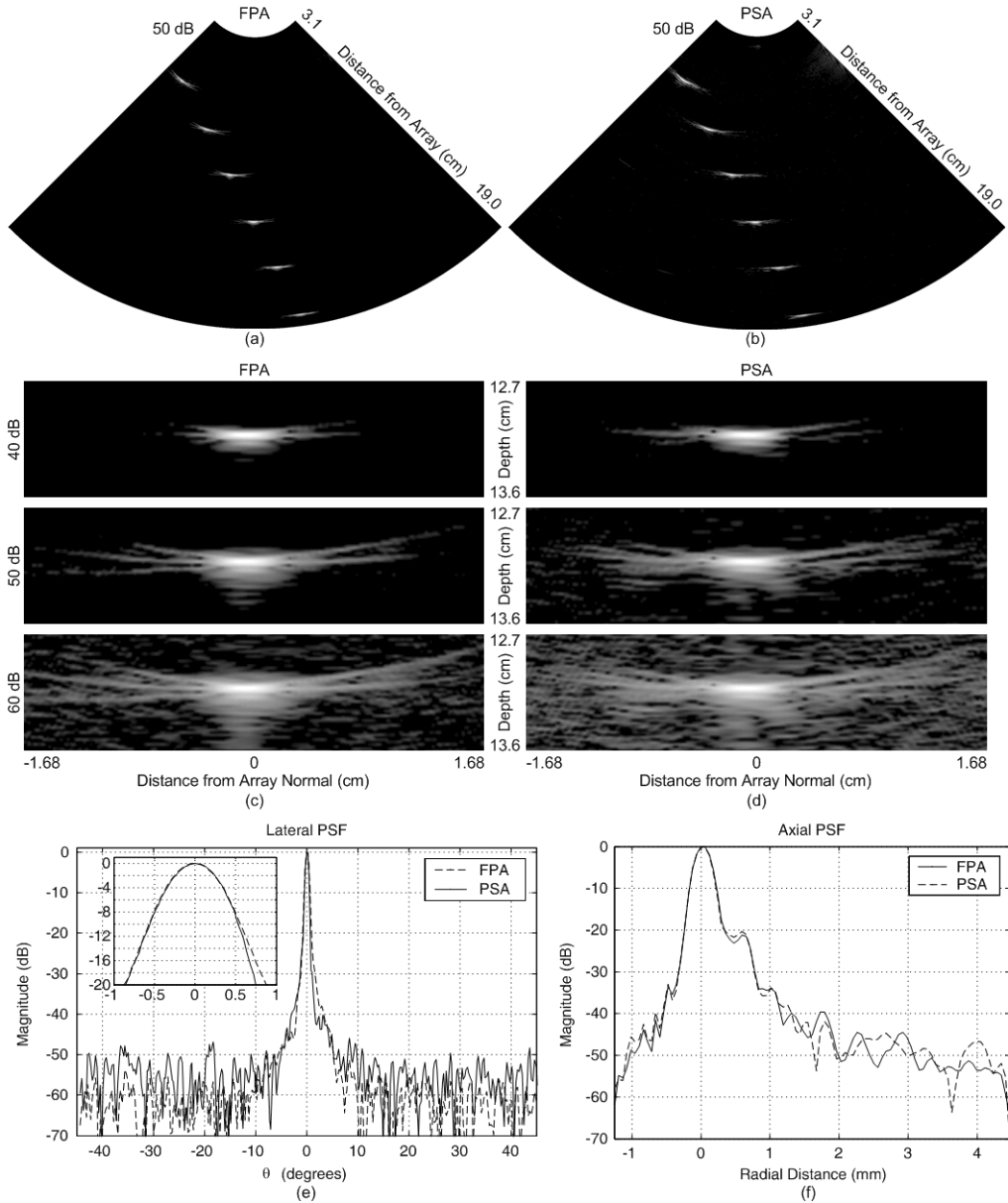
Fig. 11. Comparison of FPA and PSA imaging using experimental data. For both methods, the fixed transmit focus corresponds to the fourth wire target, and dynamic focusing is used on receive. (a) FPA image formed with 361 beams using all 128 CMUT elements. (b) PSA image formed using 5, 32-element subarrays, each acquiring 91 beams. (c) and (d) Magnification of the fourth wire target shows that the 2-D PSF for PSA imaging closely approximates that of FPA imaging. (e) Lateral PSFs of FPA and PSA, with an inset showing a close-up of the main lobe. (f) Axial PSFs for both PSA and FPA.

the near field and focal region. The data shown indicates a trend of decreasing variation with increasing subarray size.

The FPA-normalized axial resolution is shown in Fig. 12(b) and (d). Note that the vertical scale on these graphs is much smaller than that of the lateral resolution. Fig. 12(d) shows that, for the three points nearest the focal point, the axial resolution was between that of FPA and CSA for all subarray sizes. The axial resolution improved slightly for points further from the array. Fig. 12(b) emphasizes the uniformity of the axial resolution as a function of the subarray size. The mean axial resolution for

all subarray sizes was within 2% of the FPA axial resolution.

3. Subarray Size and SNR: The SNR results for varying subarray sizes are shown relative to those of FPA at each target in Fig. 13. Fig. 13(b) shows the average SNR for all subarray sizes for each target and indicates that the relative SNR was virtually constant for all points in the image. It was shown in [1] that the image SNR for PSA imaging is expected to increase as the subarray size increases:

$$SNR_{\text{PSA}} = 10 \log \left(M \sqrt{KM} \right) + SNR_0. \tag{1}$$

TABLE IV
COMPARISON OF RESULTS FOR FPA, CSA, AND PSA.

|	Parameter	Absolute			Normalized to FPA		
		FPA	PSA	CSA	FPA	PSA	CSA
	No. of front-end channels	128	32	1	100%	25%	0.8%
	No. of firings per array/subarray	361	91	126	100%	18%	25%
	No. of firings per frame	361	637	126	100%	125%	25%
	Frame rate (frames/s)	15	9	43	100%	57%	287%
Focal point (fourth target)	6-dB lateral resolution (°)	0.86	0.77	0.86	100%	90%	100%
	6-dB axial resolution (mm)	0.31	0.31	0.32	100%	100%	103%
	Image SNR (dB)	68	62	41	0	−6	−27
Mean of (all points)	6-dB lateral resolution (°)	1.07	1.65	0.88	100%	154%	82%
	6-dB axial resolution (mm)	0.33	0.32	0.32	100%	97%	97%
	Image SNR (dB)	63	48	41	0	−5	−22
	CNR[1], 4-mm cyst	3.4	3.4	2.4	100%	100%	71%
	CNR[1], 8-mm cyst	5.4	4.8	2.8	100%	90%	52%

[1]Measured from simulated data.
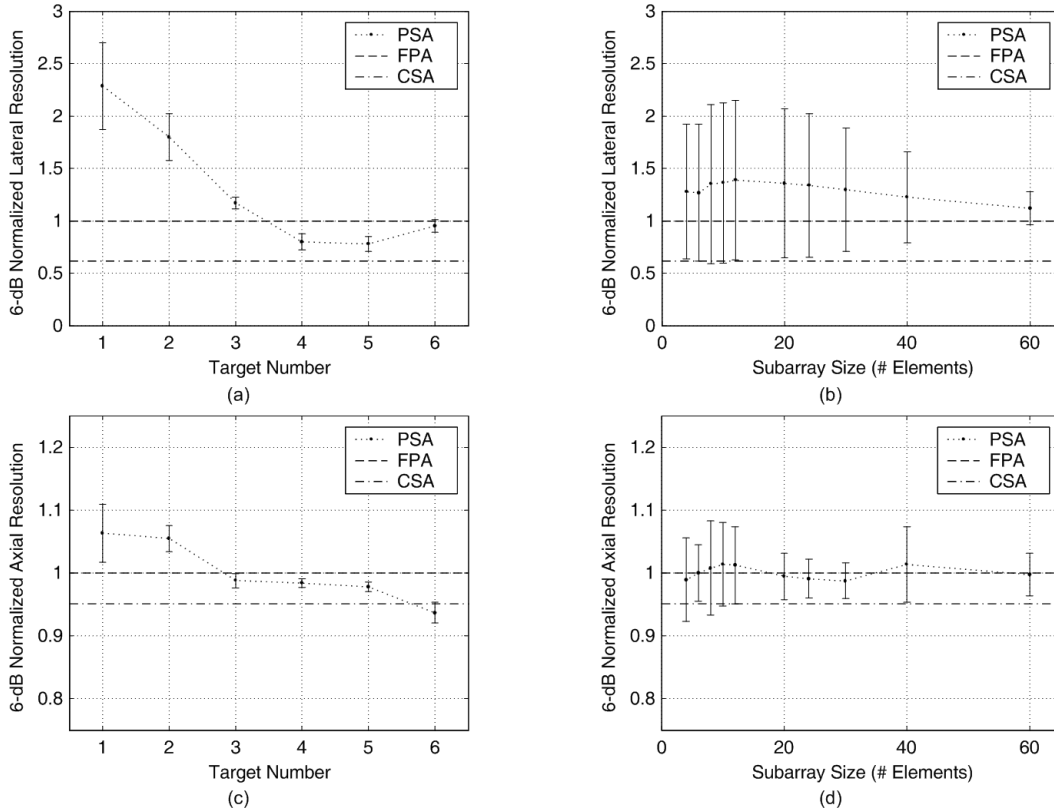
Fig. 12. Comparison of (a) and (b) lateral and (c) and (d) axial resolution for PSA, FPA, and CSA imaging using a 120-element array. All results are normalized with respect to the FPA resolution. (a) and (c) Show the mean resolutions at each target for all subarray sizes. (c) and (d) Show the mean resolutions over all targets for each PSA configuration.

This relationship is verified in Fig. 13(a), which shows the average SNR over all points in the image as a function of subarray size. The SNR for the different subarray sizes nearly spanned the entire range of the SNR of CSA to that of FPA. This behavior illustrates how PSA imaging provides the designer a trade-off between the number of channels in the phased-array system and the image SNR.

Depending on the type of power limitation imposed on the system, it may be possible to reduce the difference be-tween the SNR of PSA imaging and that of FPA imaging. The results reported here assumed that per-channel power was limited, and each element was transmitted at maximum power for all imaging modalities. Instead, if the total power is limited by the mechanical index (MI) or the spatial peak temporal average (SPTA), then the per-channel power used for PSA imaging can be increased relative to FPA per-channel power such that the MI or SPTA are equal. This increased signal power would result in an SNR improvement for PSA imaging.
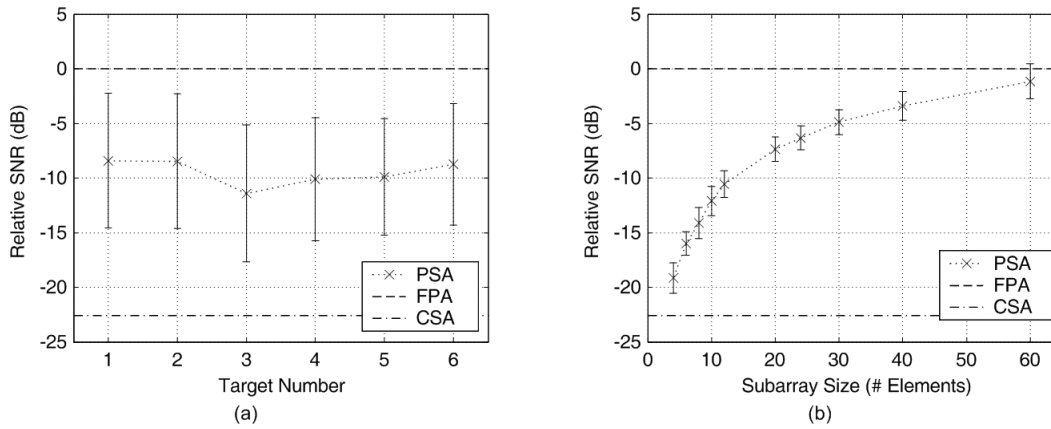
Fig. 13. SNR relative to FPA imaging measured from 120-element array experimental data. (a) Mean SNR over all subarray sizes for each of the targets. (b) Mean SNR for all six targets with PSA results for a number of different subarray sizes.

IV. CONCLUSIONS

Phased subarray imaging is a coherent array imaging method intended to significantly reduce the number of front-end electronic channels as compared to FPA imaging. We have presented a method for designing 1-D and 2-D filters for use in narrowband and wideband PSA systems, respectively. Guidelines for selecting the PSA system parameters—size and number of subarrays, filter sizes, and the upsampling rate—have been provided based on how they affect the 2-D PSF of a simulated system.

Application of PSA imaging to experimental data demonstrated the theoretical and simulated expectations. Using data from a 128-element, 1-D array, we compared the performance of a PSA system using 32-element subarrays to an FPA system using all 128 elements. Compared to FPA, PSA had little or no effect on the axial resolution. At points near the fixed transmit focal region, the lateral resolution was improved slightly, but it worsened at distances far from the focal zone. This may be compensated by multiple transmit focal zones. Reduction of the front-end hardware complexity by four was achieved at the cost of increased frame rate and slightly reduced SNR and CNR. The frame rate was reduced by 43%, and the SNR and CNR were decreased by 4.9 dB and 10%, respectively. These reductions in frame rate, SNR, and CNR are acceptable for many applications, and the resulting savings in front-end hardware can make possible phased-array imaging systems with a very large channel count or with size constraints. The effects of f/# and object motion on PSA imaging performance were not explicitly studied here and will require further investigation.

One of the primary advantages of using PSA imaging is the flexibility of trading between front-end hardware complexity, frame rate, and image quality. Hardware complexity is adjustable by selecting the number of elements per subarray. We have shown that this has a small effect on the resolution within the focal region and a more significant impact on SNR and CNR. In addition, frame rate can be reduced to achieve improved SNR by either acquiring multiple images per subarray, or using alternate transmit/receive subarray combinations as discussed in [1].

REFERENCES

[1] J. A. Johnson, M. Karaman, and B. T. Khuri-Yakub, "Coherent array imaging using phased subarrays—Part I: Basic principles," *IEEE Trans. Ultrason., Ferroelect., Freq. Contr.*, vol. 52, no. 1, pp. 31–50, 2005.

[2] Ö. Oralkan, A. S. Ergun, J. A. Johnson, M. Karaman, U. Demirci, K. Kaviani, T. H. Lee, and B. T. Khuri-Yakub, "Capacitive micromachined ultrasonic transducers: Next-generation arrays for acoustic imaging?," *IEEE Trans. Ultrason., Ferroelect., Freq. Contr.*, vol. 49, no. 11, pp. 1596–1610, 2002.

[3] L. Marple, Jr., "Computing the discrete-time 'analytic' signal via FFT," *IEEE Trans. Signal Processing*, vol. 47, no. 9, pp. 2600–2603, 1999.

[4] H. E. Karrer and A. M. Dickey, "Ultrasound imaging: An overview," *Hewlett-Packard J.*, vol. 34, no. 10, pp. 3–6, 1983.

[5] M. Karaman, L. Pai-Chi, and M. O'Donnell, "Synthetic aperture imaging for small scale systems," *IEEE Trans. Ultrason., Ferroelect., Freq. Contr.*, vol. 42, no. 3, pp. 429–442, 1995.

[6] B. Robinson and C. Cooley, "Synthetic dynamic transmit focus," in *Proc. IEEE Ultrason. Symp.*, vol. 2, pp. 1209–1214, 2000.

[7] C. R. Cooley and B. S. Robinson, "Synthetic focus imaging using partial datasets," in *Proc. IEEE Ultrason. Symp.*, Cannes, France, 1994, vol. 3, pp. 1539–1542.

[8] T. Rastello, D. Vray, and J. Chatillon, "Spatial under-sampling of ultrasound images using Fourier-based synthetic aperture focusing technique," presented at *Proc. IEEE Ultrason. Symp.*, Toronto, ON, Canada, 1997, vol. 1, pp. 823–826.

[9] T. K. Song and J. F. Greenleaf, "Ultrasonic dynamic focusing using an analog FIFO and asynchronous sampling," *IEEE Trans. Ultrason., Ferroelect., Freq. Contr.*, vol. 41, no. 3, pp. 326–332, 1994.

[10] B. Haider, "Synthetic transmit focusing for ultrasonic imaging," presented at *Proc. IEEE Ultrason. Symp.*, San Juan, Puerto Rico, 2000, vol. 2, pp. 1215–1218.

[11] M. H. Bae, M. K. Jeong, T. K. Song, and Y.-B. Ahn, "Experimental study of transmit synthetic focusing combined with receive dynamic focusing in B-mode ultrasound imaging systems," in *Proc. IEEE Ultrason. Symp.*, 1999, vol. 2, pp. 1261–1264.

[12] S. Freeman, L. Pai-Chi, and M. O'Donnell, "Retrospective dynamic transmit focusing," *Ultrason. Imag.*, vol. 17, no. 3, pp. 173–196, 1995.

Jeremy A. Johnson (S'92) received his B.S. in electrical engineering and a minor in mathematics with honors from Walla Walla College, College Place, Washington, in 1997. He received his M.S. and Ph.D. in 1999 and 2003, respectively, in electrical engineering from Stanford University, Stanford, California. He completed the Biodesign Innovation Fellowship at Stanford University in 2004. Jeremy is a Senior R&D Engineer at Medtronic Vascular, Santa Rosa, CA.

He has several summers of industry experience. He worked as a software engineer at Interactive Northwest, Inc., Tualatin, OR, during the summer of 1995; worked as an ASIC design engineer at Intel, Inc., Hillsboro, OR, during the summers of 1996 and 1997; performed research in color science at Sony Research Laboratories, San Jose, CA, during the summer of 1998; performed research in computer vision at Hughes Research Laboratories, Malibu, CA, during the summer of 1999; and developed an endoscopic calibration routine for image-enhanced endoscopy at Cbyon, Inc., Palo Alto, CA, during the summer of 2000. His research interests include medical imaging, computer-aided diagnosis, and surgical navigation systems.

Ömer Oralkan (S'93) was born in Izmit, Turkey, in 1973. He received the B.S. degree from Bilkent University, Ankara, Turkey, in 1995, and the M.S. degree from Clemson University, Clemson, SC, in 1997, and a Ph.D. degree from Stanford University, Stanford, CA, in 2004, all in electrical engineering.

From 1995 to 1996, he was a hardware and network engineer at Bilkent University Computer Center, Ankara, Turkey. In the summer of 1997, he worked as a process engineer at the National Semiconductor Research Laboratories, Santa Clara, CA. Currently, he is an engineering research associate at the Edward L. Ginzton Laboratory at Stanford University, Stanford, CA. His past and present research interests include analog and digital circuit design, micromachined sensors and actuators, and semiconductor device physics and fabrication. His current research focuses on the design and implementation of integrated ultrasonic imaging systems.

He is a corecipient of the Best Paper award presented at the IEEE International Symposium on the Physical and Failure Analysis (IPFA). He also received the 2002 Outstanding Paper Award of the IEEE Ultrasonics, Ferroelectrics, and Frequency Control Society. Dr. Oralkan is a member of the IEEE.

A. Sanlı Ergun (S'96–A'98–M'99) was born in Ankara, Turkey, in 1969. He received his B.Sc., M.Sc., and Ph.D. degrees in 1991, 1994, and 1999, respectively, all in electrical and electronics engineering, from Bilkent University, Ankara, Turkey.

He was a research assistant in Bilkent University, Ankara, Turkey, between 1991 and 1999. He now is in the E. L. Ginzton Laboratory, Stanford University, Stanford, CA, as an engineering research associate. His research interests are microwave electronics, ultrasonics, microelectricalmechanical systems (MEMS), and specifically capacitive micromachined ultrasound transducers (CMUTs). He is a member of the IEEE and the Electron Devices Society.

Utkan Demirci (S'01) received his B.S. degree from the University of Michigan, Ann Arbor, in 1999 with Summa Cum Laude, supported by the Full Presidential Scholarship from Turkish Ministry of Education, and the M.S. degree from Stanford University, Stanford, CA, in 2001, both in electrical engineering. He currently is pursuing a Ph.D. degree in electrical engineering from Stanford University.

His research interests are design of 1-D and 2-D capacitive micromachined ultrasound transducer (CMUT) arrays for medical ultrasound imaging, and micromachined flextensional transducers for high resolution printing and ejection applications.

Mustafa Karaman (S'88–S'89–M'89–M'93–M'97) was born in Balıkesir, Turkey, in 1964. He received the B.Sc. degree from the Middle East Technical University, Ankara, Turkey, and the M.Sc. and Ph.D. degrees from Bilkent University, Ankara, Turkey, in 1986, 1988, and 1992, respectively, all in electrical and electronics engineering.

From 1993 to 1994, he was a post-doctoral fellow in the Biomedical Ultrasonics Laboratory in the Bioengineering Department, University of Michigan, Ann Arbor. From 1995 to 1996, he was on the faculty with the Electrical and Electronics Engineering Department of Kırıkkale University, Kırıkkale, Turkey, first as assistant professor and later as associate professor. In 1996, he joined Başkent University, Ankara, Turkey, as the Chairman of the Electrical and Electronics Engineering and Acting Chairman of the Computer Engineering Department and served in founding these departments. He was a visiting scholar in the Biomedical Ultrasonics Laboratory at the University of Michigan, Ann Arbor, and in the E. L. Ginzton Laboratory at Stanford University, Stanford, CA, in the summer terms of 1996–1997 and 1999, respectively.

Between 2000–2002, he was with the E. L. Ginzton Laboratory at Stanford University as a visiting faculty in electrical engineering. In 2002, he joined Işık University, Istanbul, Turkey, where he is currently working as faculty in electronics engineering.

In 1996, he was awarded H. Tuğaç Foundation Research Award of Turkish Scientific and Technical Research Council for his contributions to ultrasonic imaging. His research interests include signal and image processing, ultrasonic imaging and integrated circuit design. Dr. Karaman is a member of the IEEE.

Butrus T. Khuri-Yakub (S'70–S'73–M'76–SM'87–F'95) was born in Beirut, Lebanon. He received the B.S. degree in 1970 from the American University of Beirut, Beirut, Lebanon, the M.S. degree in 1972 from Dartmouth College, Hanover, NH, and the Ph.D. degree in 1975 from Stanford University, Stanford, CA, all in elecrical engineering.

He joined the research staff at the E. L. Ginzton Laboratory of Stanford University in 1976 as a research associate. He was promoted to a senior research associate in 1978 and to a professor of electrical engineering (research) in 1982. He has served on many university committees in the School of Engineering and the Department of Electrical Engineering at Stanford University. Presently, he is the Deputy Director of the E. L. Ginzton Laboratory.

Dr. Khuri-Yakub has been teaching at both the graduate and undergraduate levels for over 15 years. His current research interests include in situ acoustic sensors (temperature, .1m thickness, resist cure, etc.) for monitoring and control of integrated circuits manufacturing processes, micromaching silicon to make acoustic materials and devices such as airborne and water immersion ultrasonic transducers and arrays, and fluid ejectors, and in the field of ultrasonic nondestructive evaluation and acoustic imaging and microscopy.

Dr. Khuri-Yakub is a fellow of the IEEE, a senior member of the Acoustic Society of America, and a member of Tau Beta Pi. He is associate editor of Research in Nondestructive Evaluation, a Journal of the American Society for Nondestructive Testing. He has authored over 400 publications and has been principal inventor or coinventor of 61 issued patents. He received the Stanford University School of Engineering Distinguished Advisor Award, June 1987, and the Medal of the City of Bordeaux for contributions to NDE, 1983.